Microstructure of as cast reinforced ductile iron

M. Martinez Celis*[1], N. Valle[1], J. Lacaze[2], I. O. Thorbjornsson[3], B. Johannesson[3] and J. T. Thorgrimsson[4]

Local hardening of parts made of ductile iron may be achieved by having carbides appearing in appropriate locations. The present work focuses on the study of the as cast microstructure of parts reinforced by Cr containing steel inserts. The presence of such inserts in the mold cavity results in localised chemical changes during the casting process, constituents of the insert (principally chromium) being transferred to the cast iron while carbon penetrates the insert. This leads to the formation of various carbides within and in the surroundings of the insert.

Keywords: Microstructure, Local reinforcement, Ductile cast iron, Chromium carbides

Introduction

Ductile irons are essentially ternary Fe–C–Si alloys with carbon and silicon contents in the ranges 3·4–3·9 and 1·8–2·8 wt-% respectively. In ductile iron, graphite is in the form of nodules due to the addition of spheroidising elements, usually magnesium. The majority of the castings produced with nodular cast irons has a pearlitic, a ferritic or a ferritic–pearlitic matrix in as cast state[1,2] and presents a ductility (or strength) that increases (or decreases) when the ratio of ferrite over pearlite increases. On the other hand, white cast irons and high chromium cast irons have high abrasion resistance because of the presence of carbides (M_3C and/or M_7C_3) but are brittle.[3–6] A combination of these two materials thus appears highly appropriate when the wear and tear are localised so that it is not necessary to have a whole component with high wear resistance, i.e. when localised abrasion resistance is enough.

Applications of reinforced ductile irons, in particular surface hardened parts, are found in automotive industry (pistons for compressors, gears, crankshafts, etc.) as well as in mining, fishing or agriculture industries. Accordingly, efforts have been made since a long time in order to improve locally the wear resistance of ductile iron, e.g. by laser surface modification, boriding or nitriding.[7–10] A more versatile and less costly route would be to include the reinforcement as part of the casting process. Innovation Center Iceland (ICI) and Málmsteypa Thorgríms Jónssonar (MTJ, Foundry of Thorgrimur Jonsson) have already demonstrated that casting of ductile iron with localised reinforcement is possible.[11] It has been shown that with the right combination of temperature and composition of the melt, appropriate alloying elements and thickness of component, parts can be cast with local reinforcement. The principle of the method is to fix chromium containing inserts in strategic locations in the mould in order to induce the formation of carbides during solidification of the casting. The technique was developed by ICI and MTJ in the early 1990s, but their work was not published in the open literature. Since then, as far as the authors know, only one reference has been published on local reinforcement of ductile iron with inserts.[12] Qian *et al.*[12] compared the capabilities of ferritic and austenitic steel inserts introduced in ductile cast iron parts, and reported that austenitic steel gives much better results because of its lower melting point and a better surface bonding.

The present study focuses on the characterisation of the as cast microstructure of ductile iron reinforced with steel inserts. It is not intended to discuss the optimisation of the process, but rather to gain a better understanding of the process by which reinforcing of ductile iron is achieved. The as cast microstructure has thus been investigated by means of various complementary methods, including optical microscopy, scanning (SEM) and transmission (TEM) electron microscopies with energy dispersive spectrometry (EDS) and secondary ion mass spectrometry (SIMS).

Materials and methods

Materials

The samples observed in this study are specimens taken out from reinforced parts cast by ICI and MTJ following the process described in the corresponding patent.[11] In the present case, the inserts were made of stainless steel, i.e. Fe–Ni–Cr alloy containing about 16–20 wt-%Cr, 8 wt-%Ni and small amounts of manganese and silicon. These inserts were appropriately located in the mould cavity, depending on where high wear resistance is required for the final part. Their thickness (typically 1–2 mm) and

[1]Department of 'Science and Analysis of Materials' (SAM), Centre de Recherche Public-Gabriel Lippmann 41 rue du Brill, L-4422 Belvaux, Luxembourg
[2]CIRIMAT, Université de Toulouse, ENSIACET, BP 44632, 31030 Toulouse Cedex 4, France
[3]Innovation Center Iceland, Keldnaholt, 112 Reykjavik, Iceland
[4]Malmsteypa Thorgrims Jonssonar, Midhraun 6, 210 Gardabaer, Iceland

*Corresponding author, email mayemartinez@yahoo.com

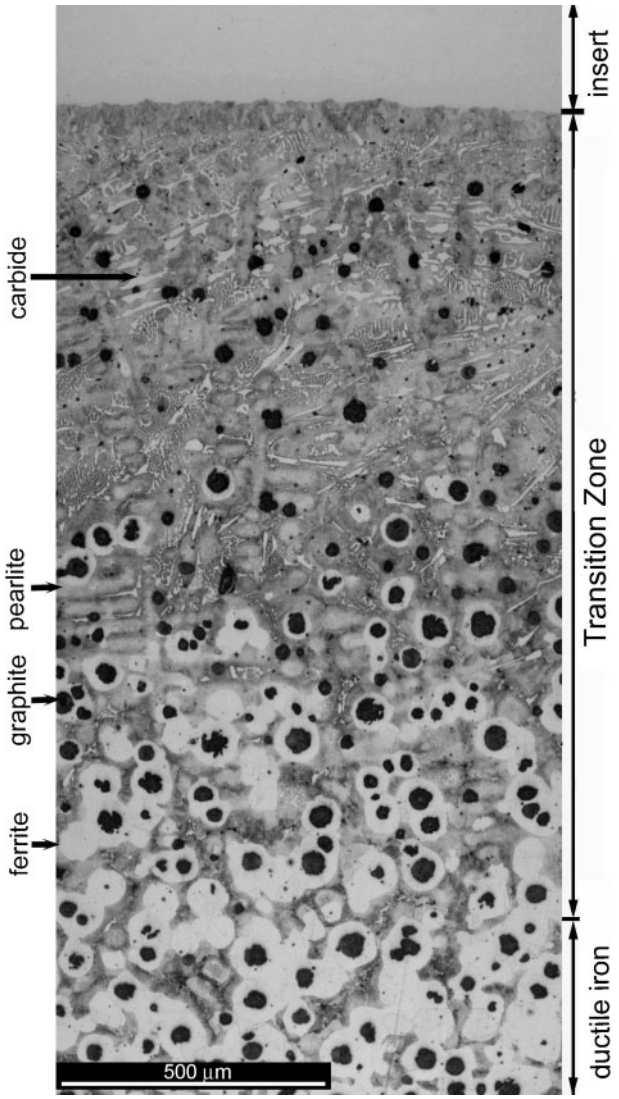

1 Optical micrograph of as cast sample showing insert, transition zone (TZ) and bulk ductile iron (etched with 4% nital)

size (typically 5–10 cm) depend on the geometry and size of the final component. The cast used in the present study is an unalloyed standard nodular cast iron (C: 3·7–3·9 wt-%; Si: 2·7–2·8 wt-%; Mn: 0·12–0·16 wt-%; Mg: 0·03 wt-%; Cu: $27{\cdot}6\times10^{-3}$–$42{\cdot}6\times10^{-3}$ wt-%; Ni: $26{\cdot}8\times10^{-3}$–$34{\cdot}5\times10^{-3}$ wt-%; P: $21{\cdot}9\times10^{-3}$–$26{\cdot}5\times10^{-3}$ wt-%; S: $10{\cdot}9\times10^{-3}$–11×10^{-3} wt-%; Mo: $<0{\cdot}1\times10^{-3}$ wt-%). The superheat of the melt before pouring in the mould was adjusted to

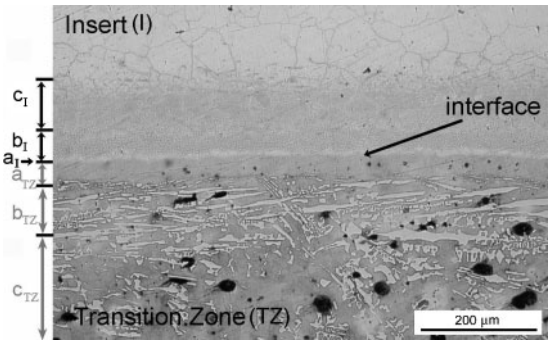

2 Optical micrograph of region around insert/transition zone interface (etched with Villela)

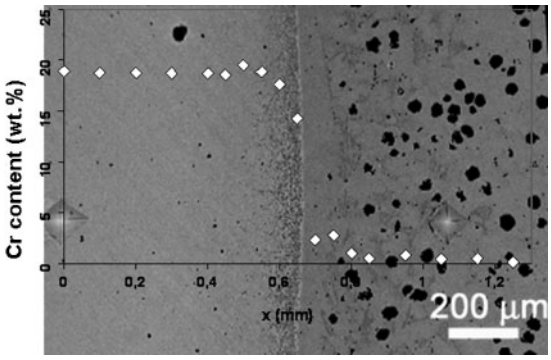

3 Example of EDS analysis of chromium across interface between insert and cast iron

the size of the cast part so as to ensure partial dissolution of the inserts before solidification of the cast iron.

Analytical techniques

Sample preparation for optical metallographic observation was carried out using standard techniques. The surface of the samples was polished down to 1 µm using diamond paste before chemical etching. Samples microstructure was successfully revealed using 4% nital (96 vol.-% ethanol and 4 vol.-% nitric acid) and Glyceria also named Villela (two parts by volume of glycerol, two parts of hydrochloric acid and one part of nitric acid). Etching time was a few seconds in the case of nital and around 1 min with Villela. The observations were achieved using a Leica DM LM optical microscope; they allowed locating the inserts and estimating the extent of the zones around the inserts showing microstructure differences with respect to nodular iron in the bulk of the casting.

The scanning electron microscope used was Leica Stereoscan 430i operated at 20 kV. The samples were polished before observation in order to eliminate any etching traces. SEM was mainly used for imaging the microstructure by means of the differences in chemical contrast between phases. Chemical analyses were also performed in the SEM using EDS (Oxford Isis 200).

Microstructure characterisation was complemented by TEM with a LEO 922 OMEGA operating at 200 kV that was used for both imaging and electron diffraction. Thin foils were prepared by mechanical polishing disc specimens of 3 mm in diameter down to 100 µm. Then, a precision dimple grinder instrument was used to reduce the thickness of the disc down to 50 µm at the thinner part of the dimple. For the last step of thinning, ion milling was preferred instead of electropolishing because of the large differences between the phases present in the samples. The angles of the two ion beams in the final stage of milling were set at 6° for the best results.

To complement the chemical analyses performed with the EDS in the SEM, SIMS experiments were carried out in a CAMECA NanoSIMS 50 instrument. The

Table 1 Composition of core of insert and of zone a_I (wt-%): carbon concentration was not taken into account in composition

	Fe	Cr	Ni	Mn	Si
Core of the insert	Bal.	16·2	7·8	1·6	0·4
Zone a_I	Bal.	2·5	1·5	0·4	3·5

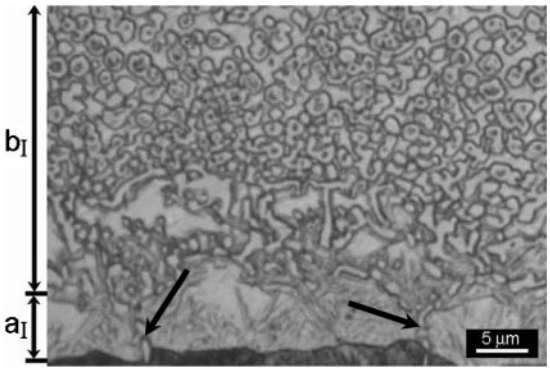

4 Optical micrograph of zones a_I and b_I after chemical overetching with Villela: arrows show grain boundaries in a_I zone

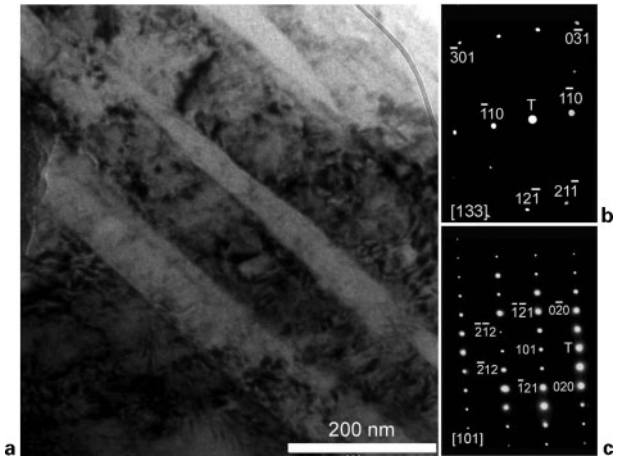

5 Zone a_I: *a* TEM image of matrix, *b* diffraction patterns of matrix, obtained from whole area, zone axis [133], and *c* diffraction patterns of carbide, zone axis [101]

instrument was operated with a Cs primary source at an energy of 16 keV. Carbon, silicon, nickel and chromium (as CrC^- ions) could thus be analysed.

Results

In all the samples observed, a perfect bonding between inserts and ductile iron was noticed. Figure 1 shows a mounting of optical micrographs from the bulk ductile iron to the centre of an insert. Chemical etching with nital reveals three well marked areas as indicated in this figure. At the bottom, the ductile cast iron exhibits a pearlite–ferrite matrix, in which pearlite (grey contrast) and nodules of graphite (dark contrast) surrounded by ferrite (light contrast) can be clearly distinguished. At the top of the optical image, there is one insert whose microstructure is not revealed by nital etching. In between the insert and the bulk ductile iron, there is a region referred to as transition zone that stretches up to 2 mm. This region is composed of pearlite, graphite and ferrite as is the bulk ductile iron, but also of coarse carbides in light contrast with various morphologies.

An enlarged view of the layer adjacent to the insert is presented in Fig. 2 that shows an optical micrograph acquired after etching with Villela. At the limit between the insert and the transition zone, there is an abrupt change in the microstructure which should be related to the interface between the inner part of the insert that remained solid and the liquid. EDS analysis in the SEM confirmed that there is a concomitant abrupt change in composition when crossing this interface, as illustrated with Fig. 3 which shows an example of chromium profile. It is of note that some chromium is anyway present on the cast iron side of the interface. The transition zone thus results certainly from the change in

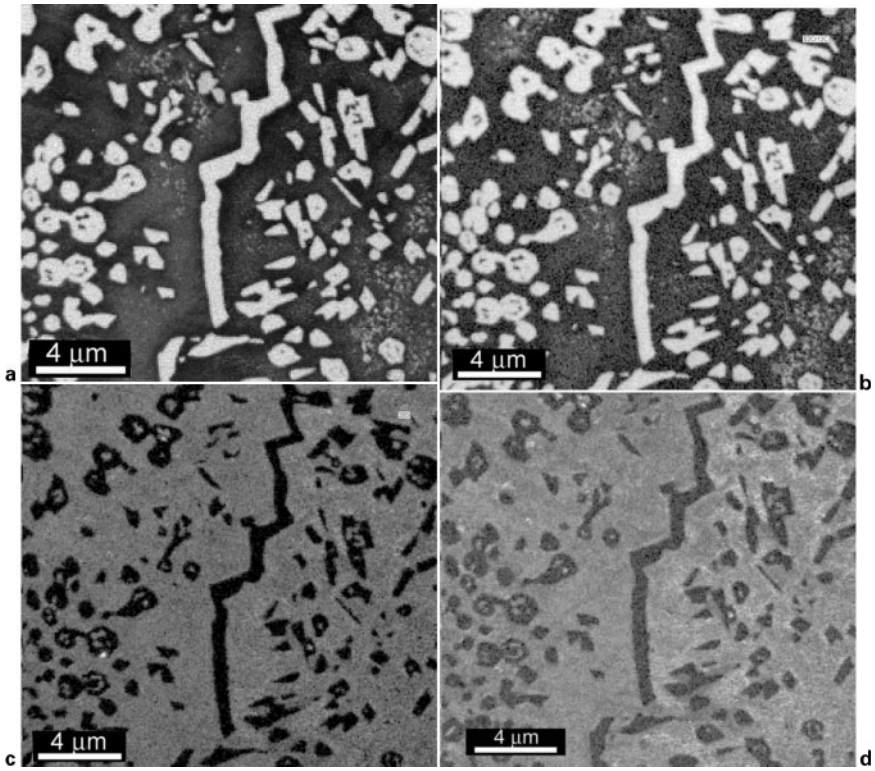

6 NanoSIMS analyses in zone b_I: distribution of *a* ^{12}C, *b* $^{52}Cr^{12}C$, *c* ^{28}Si and *d* ^{58}Ni: white contrast represents highest concentrations of element while black contrast represents lowest concentrations

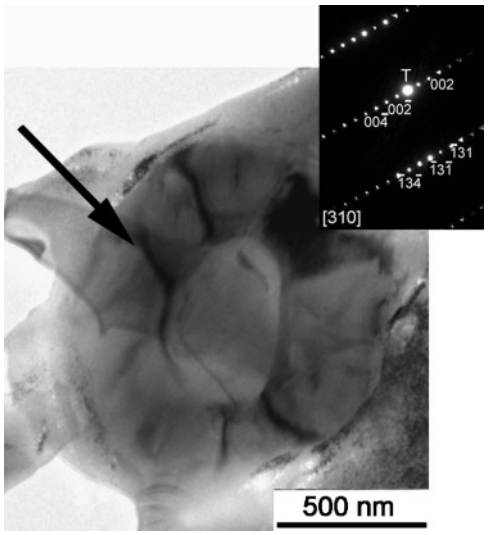

7 Analysis (TEM) of zone b_I: bright field micrograph of one round M_7C_3 carbide and diffraction pattern, zone axis [310] (arrow shows region where diffraction pattern was recorded)

chemical composition of the melt because of partial dissolution of the insert.

It is also seen in Fig. 2 that there is a microstructure gradient in the insert that did not appear after nital etching. As a matter of fact, three zones labelled a, b and c could be defined on each side of the interface on the basis of the observed changes in the microstructure. These zones are indicated in Fig. 2 where subscript I refers to the microstructure inside the insert, while subscript TZ refers to the microstructure in the transition zone. The characterisation of these various zones will be carried out starting with the insert in the next section and continuing with the transition zone in the following section.

Insert

Along the interface between the insert and the transition zone, there is a thin zone, labelled a_I (Fig. 2), clearly visible at the bottom of the enlarged micrograph in Fig. 4. It seems to be single phase, except for the presence of a fine precipitation of carbides at some grain boundaries. The thickness of this zone is ~ 5 μm. EDS analyses indicate an important difference in composition in comparison to the core of the insert, the zone a_I being richer in Si and much poorer in Cr, Ni and Mn than the insert (Table 1). In addition, TEM observation evidences a structure similar to martensite (Fig. 5*a*) and the diffraction patterns confirm that the structure corresponds to the body centre cubic Fe-α (Fig. 5*b*). Diffraction patterns of the carbides showed them to be of the M_3C type (Fig. 5*c*).

In the adjacent region within the insert, labelled b_I, carbides are present along grain boundaries, but also as small and round precipitates inside the grains (Fig. 4). SEM observations in backscattered mode revealed that these latter carbides have a heterogeneous chemical distribution and consist of at least two phases. Additional information concerning composition in this zone was provided by NanoSIMS analyses which reveal the spatial distribution of carbon, chromium bearing carbides (through the association of Cr and C), silicon and nickel (Fig. 6). The external part of these precipitates has a uniform distribution in carbon and chromium, while no carbon was detected in the core of these precipitates, where elements such as silicon and nickel are present. The diffraction patterns reveal that these ring-shaped carbides correspond to M_7C_3 type carbides (Fig. 7).

Further in the insert, there is a zone c_I where carbides present various features (Fig. 2). Most of them are intragranular and have a structure finer than those in zone b_I and are not clearly defined under optical microscopy (Fig. 8*a*). In some regions as in Fig. 8*a*, there is a lamellar two-phase precipitation forming cells that can reach up to 20 μm. Like in zone b_I, carbides are also present at grain boundaries and are associated to a precipitation free zone along all grain boundaries (black arrows in Fig. 8*a*).

The characteristics of the small intragranular carbides are more clearly visible in backscattered mode in the SEM: they are either round or plate-like, and many have facets (Fig. 8*b*). TEM observations confirmed that there carbides are facetted and that their size can be as small as 50 nm. Electron diffraction patterns of the carbides found in zone c_I could all be indexed according to the $M_{23}C_6$ structure, and evidenced epitaxy of the precipitates with the matrix (Fig. 9). Finally, NanoSIMS analyses revealed a uniform distribution of Cr, C, Si and Ni in all the carbides present in this zone.

Transition zone

In the transition zone, three regions labelled a_{TZ}, b_{TZ} and c_{TZ} have also been distinguished (Fig. 2). Figure 10 shows typical examples of the microstructure observed in the zones a_{TZ} and b_{TZ}. The region adjacent to the interface (a_{TZ}) consists only in pearlite, and its thickness can go up to 100 μm. In the next region (b_{TZ}), the material consists in coarse carbides within a pearlite

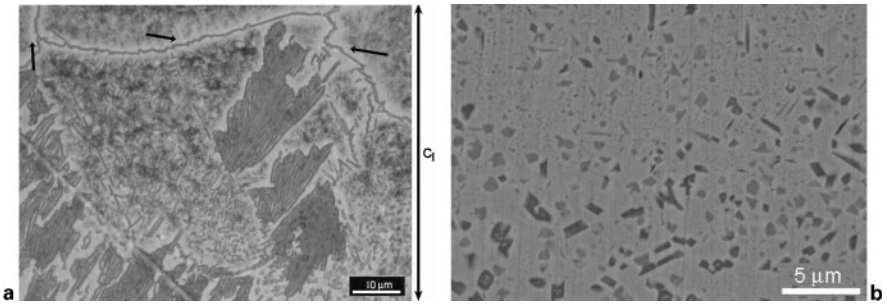

8 Zone c_I: *a* optical micrograph showing small intragranular carbides, carbides at grain boundaries, precipitation free zone (arrows) and big lamellar carbides (etched with Villela) and *b* backscattering electron image showing morphology of small carbides inside grains

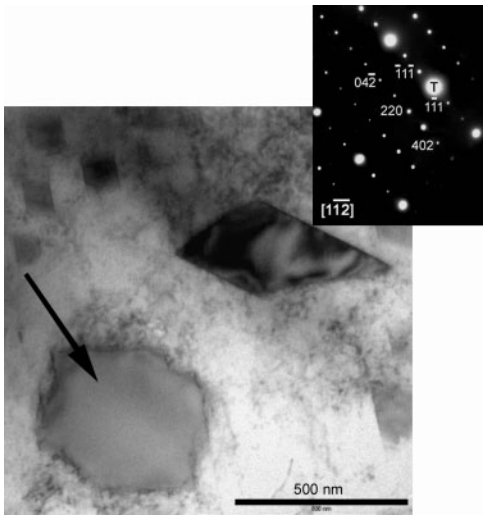

9 Analysis (TEM) of zone c_t: bright field micrograph of $M_{23}C_6$ carbides (arrow shows region where diffraction pattern was recorded) and diffraction pattern showing epitaxy relationship of carbide and matrix, zone axis $[1\bar{1}2]$

matrix. Close to the a_{TZ} zone, these carbides appear either as equiaxed cells (Fig. 10*a*) or present the characteristic features of ledeburite (Fig. 10*b*) in which the carbide is cementite. Both types of carbides have certainly precipitated during a eutectic reaction with liquid and austenite, this latter then transforming to pearlite during cooling after solidification.

The carbides in the zone b_{TZ} are different not only in morphology but also in composition as evidenced by the backscattered electron image in Fig. 11. Those in the equiaxed cells, which are always located near the insert, are small and appear in dark contrast. The others, most often further away from the interface as in Fig. 10, are less contrasted compared to the matrix. EDS analyses indicate that the darkest carbides contain significantly more chromium (Fe/Cr=2) than the others (Fe/Cr=15). Moreover, the examination of the transition zone by electron diffraction evidences the presence of two types of carbides, namely, M_3C and M_7C_3. M_7C_3 carbides are only present in zone b_{TZ} while M_3C carbides appear all through the zones b_{TZ} and c_{TZ}. It is of note that the extension of zone a_{TZ} in Fig. 10*b* is much larger than in Fig. 10*a* and this is associated with the absence of M_7C_3.

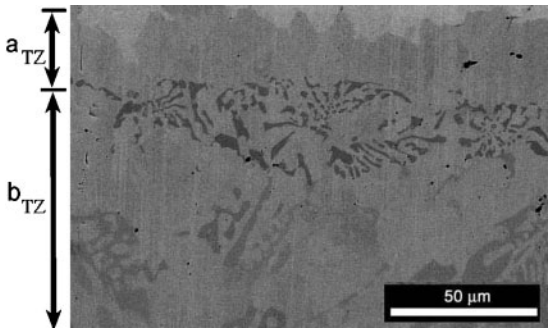

11 Backscattered electron image showing two types of carbides in transition zone

This is certainly due to slight change in the melt composition along the insert/liquid interface at the time the solidification started.

The distribution of C and Cr inside the two types of carbides was found to be uniform by NanoSIMS imaging, and it was noted that they are silicon free. This is illustrated in Fig. 12 for the low chromium bearing carbides, where it is also observed that the pearlite of the matrix is nicely defined on C and CrC maps.

Further away from the interface (zone c_{TZ}, Fig. 2), there is a continuous evolution of the microstructure: near the b_{TZ} zone, the region is composed of pearlite, carbides and small graphite nodules, smaller than in the bulk of the ductile cast iron and without a ferrite shell. As one moves away from the insert, the nodules become bigger, the fraction of carbides diminishes and ferrite appears as a constituent of the microstructure. At a distance of around 2 mm from the insert, the microstructure is similar to that of the bulk ductile cast iron, consisting in pearlite, ferrite and graphite.

Discussion

These results show that the introduction of inserts induces the formation of carbides not only in the transition zone but also inside the insert. This is due to an opposite flux of elements during the casting process, carbide former (chromium and to a lesser extent manganese) entering the liquid cast iron by partial dissolution of the insert, while carbon diffuses from the melt into the solid insert. After pouring of the melt, the carbon content at the outer surface of the inserts

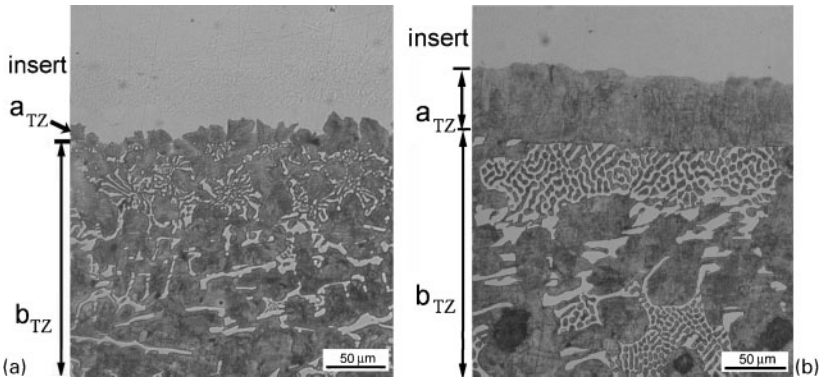

10 Optical micrographs showing pearlite and different types of eutectic carbides in light contrast: *a* M_7C_3 forming equiaxed cells (top of the b_{TZ} zone) and M_3C with blocky morphology (bottom of b_{TZ} zone) and *b* M_3C forming regularly patterned ledeburite (both top and bottom of the b_{TZ} zone)

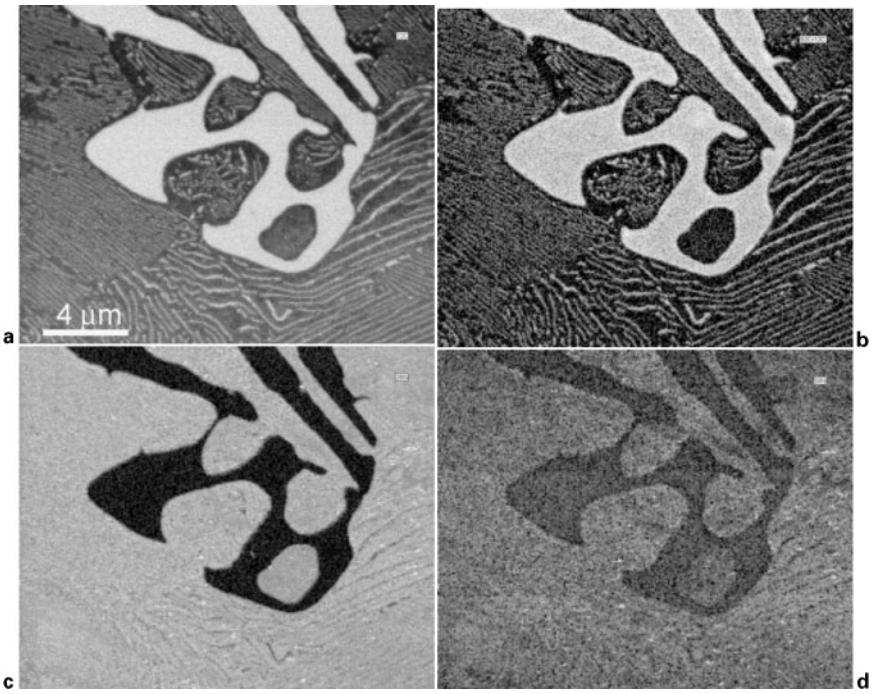

a ^{12}C; *b* $^{52}Cr^{12}C$; *c* ^{28}Si; *d* ^{58}Ni

12 NanoSIMS images of carbides with low chromium level in zone b_{TZ} white contrast represents highest concentrations of element while black contrast represents lowest concentrations

increases rapidly. While the carbon diffuses towards the core of the insert, carbon saturation at the interface is reached and the external part of the insert dissolves. This process is expected to be continuous and to lead to a local change in composition of the melt by enrichment in Cr, Mn and Ni. This dissolution process stops when the melt solidifies because of the cooling.

The formation of carbides inside the insert is essential to the success of the reinforcement.[11] The time t necessary for carbon atoms to reach the core of the insert can be estimated with the relation $t \approx L^2/D$, where L is the distance over which diffusion has to take place while D is the carbon diffusion coefficient. By considering an average temperature of 1300°C for the casting and solidification process, expressing the diffusion coefficient of carbon in austenite[13] as $D=2{\cdot}345 \times 10^{-5}\exp(-17767/T)$ m^2 s^{-1} and taking for the diffusion length $L=0{\cdot}5$ mm, t is found equal to 1·5 min. Such a value is well in line with the time needed to fill a sand mould and cool the melt to the solidification temperature; it thus explains the precipitation of carbides in the core of the insert.

The electron diffraction analyses reveal the presence of three types of carbides in the insert. Near to the interface, where the composition differs from that of the core with very low Cr and Ni contents, M_3C have been identified within a matrix consisting in martensite. The two other types of carbides are M_7C_3 and $M_{23}C_6$; they were respectively found in zones b_I and c_I that both have an austenite matrix. The M_3C is present in a very thin zone of ~5 µm while the other carbides are present in two successive layers each ~100 µm thick. For illustration purpose, the composition profile within the insert has been schematically drawn in Fig. 13 onto the isothermal section at 880°C of the Fe–Cr–C system, assuming that the carbon content changes from 1 to 2 wt-% from the centre to the surface of the insert, while the Cr content decreases from 16 to 2·5 wt-% (Table 1). The distribution of the phases present in the insert is in accordance with the two-phase equilibrium domains encountered along the line in Fig. 13.

It should be noted that the actual carbon content is certainly lower than the values assumed, in particular because of the presence of Ni and Si that both decrease carbon solubility in austenite. This should not change the feature depicted by Fig. 13 as all the two- and three-phase fields would be also shifted to lower carbon content.

On the other side of the interface, solidification of the transition zone leads to three different zones as already described (Fig. 2). During cooling, the insert acts as a preferential site for solidification of austenite, which may be assumed to be the first solid phase to appear as there is no nucleation barrier for it. Also during cooling, growth of the austenite layer leads to a further increase

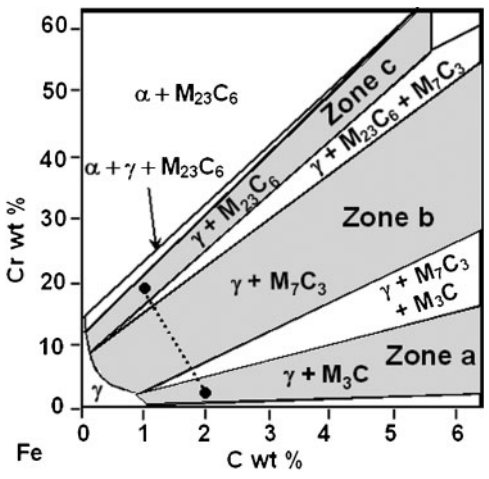

13 Isothermal section of Fe–Cr–C diagram at 880°C[14]

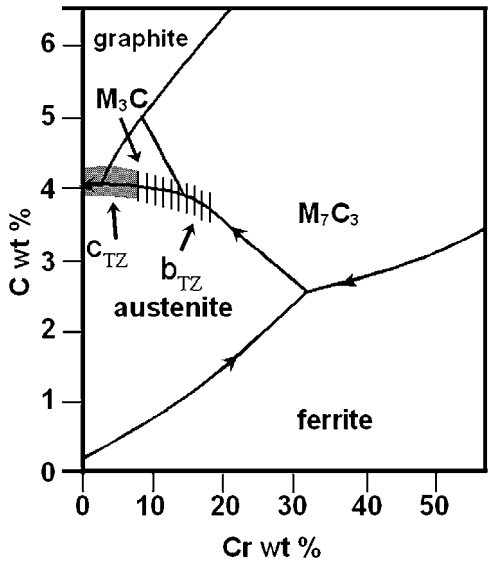

14 Liquidus projection of Fe–Cr–C[15]

in the chromium content in the adjacent liquid until a temperature is reached at which M_3C or M_7C_3 can precipitate. The M_7C_3 carbides are richer in chromium and are situated always next to the interface (Fig. 10*a*), while cementite with lower chromium content can precipitate next to the insert but also all along zones b_{TZ} and c_{TZ} (Fig. 10*b* and Fig. 11). Later, when the eutectoid transition is reached, austenite transforms into pearlite, which is the constituent that is observed at room temperature in zone a_{TZ} (Fig. 10). For illustration purpose again, the possible composition ranges during eutectic reaction of the b_{TZ} and c_{TZ} zones have been tentatively indicated along the eutectic trough of the liquidus projection of the Fe–Cr–C system (Fig. 14). The arrows along the eutectic lines show that M_7C_3 should appear before cementite upon cooling, in relation with the higher Cr content. As before, the presence of Ni and Si may change the actual Cr content along the eutectic lines but without modifying the conclusions drawn here.

Conclusions

The introduction of Cr containing inserts in the mould of parts to be cast with ductile iron is an efficient way of producing local reinforcement.[11] If the size of the inserts is such that they partly dissolve during the process, precipitation of carbides occurs both in the inserts and in the ductile iron around them. Inside the insert within the as cast parts, three different types of carbides have been observed, namely, $M_{23}C_6$ and M_7C_3 in the core and M_3C near to its outer surface. Around the inserts, a gradient microstructure is observed from the surface of the insert to the bulk ductile iron. In this transition zone, the most important change in the microstructure, when compared to that of the bulk cast iron, is the presence of eutectic carbides, M_7C_3 and M_3C. Therefore, this simple process allows local reinforcement of the parts, which could be further heat treated for optimising their wear properties.[11,16]

Acknowledgements

The authors wish to thank E. Lentzen, P. Grysan and B. El Adib for their helpful contribution to this work. This work was financially supported by the Fonds National de la Recherche de Luxembourg (DIWEAR Project within the INTER – ERA-Net MATERA Programme, FNR/MAT/06/05/01).

References

1. J. R. Davis: 'Cast irons'; 1996, Materials Park, OH, ASM International.
2. C. Labrecque and M. Gagné: *Can. Metall. Q.*, 1998, **37**, 343–378.
3. C. P. Tabrett and I. R. Sarre: *J. Mater. Sci.*, 2000, **35**, 2069–2077.
4. X. Zhi, J. Xing, Y. Gao, H. Fu, J. Peng and B. Xiao: *Mater. Sci. Eng. A*, 2008, **A487**, 171–179
5. A. Kootsookos and J. D. Gates: *J. Mater. Sci.*, 2004, **39**, 73–84.
6. S. O. Yilmaz: *J. Mater. Sci.*, 2007, **42**, 6769–6778.
7. A. Amirsadeghi and M. Heydarzadeh Sohi: *J. Mater. Process. Technol.*, 2008, **201**, 673–677.
8. J. H. Abboud, K. Y. Benyounis, A. G. Olabi and M. S. J. Hashmi: *J. Mater. Process. Technol.*, 2007, **182**, 427–431.
9. M. A. Béjar, W. Schnake, W. Saavedra and J. P. Vildósola: *J. Mater. Process. Technol.*, 2006, **176**, 210–213.
10. M. Heydarzadeh Sohi, G. Karshenas and S. M. A. Boutorabi: *J. Mater. Process. Technol.*, 2004, **153–154**, 199–202.
11. I. Ö. Thorbjörnsson and J. T. Thorgrímsson: 'Nodular iron castings', WO-2009/081420 A1, 2009.
12. M. Qian, S. Harada, Y. Kuroshima and H. Nagayoshi: *Mater. Sci. Eng. A*, 1996, **A208**, 88–92.
13. Z.-K. Liu and J. Agren: *Acta Metall.*, 1989, **37**, 3157–3163.
14. M. Durand-Charre: 'La microstructure des aciers et des fontes-Genèse et interpretation', 400; 2006, Paris, SIRPE.
15. G. V. Raynor and V. G. Rivlin: 'Phase equilibria in iron ternary alloys', 499; 1988, London, The Institute of Metals.
16. M. Martinez Celis, N. Valle, J. Lacaze, I. O. Thorbjornsson, B. Johannesson, J. T. Thorgrimsson, B. Podgornik and J. Vizintin: *Key Eng. Mater.*, 2011, **457**, 441–446.